ORIGINAL ARTICLE

Automated tilt compensation in acoustic microscopy

Shubham Kumar Gupta[1] | **Anowarul Habib**[2] | **Prakhar Kumar**[3] |
Frank Melandsø[2] | **Azeem Ahmad**[2]

[1]Department of Chemical Engineering, Indian Institute of Technology, Guwahati, India

[2]Department of Physics and Technology, UiT The Arctic University of Norway, Tromso, Norway

[3]Department of Electronics Engineering, Indian Institute of Technology, Dhanbad, India

Correspondence
Anowarul Habib, Department of Physics and Technology, UiT The Arctic University of Norway, Tromso, Norway.
Email: anowarul.habib@uit.no

Abstract
Scanning acoustic microscopy (SAM) is a potent and nondestructive technique capable of producing three-dimensional topographic and tomographic images of specimens. This is achieved by measuring the differences in time of flight (ToF) of acoustic signals emitted from various regions of the sample. The measurement accuracy of SAM strongly depends on the ToF measurement, which is affected by tilt in either the scanning stage or the sample stage. Hence, compensating for the ToF shift resulting from sample tilt is imperative for obtaining precise topographic and tomographic profiles of the samples in a SAM. In the present work, we propose an automated tilt compensation in ToF of acoustic signal based on proposed curve fitting method. Unlike the conventional method, the proposed approach does not demand manually choosing three separate coordinate points from SAM's time domain data. The effectiveness of the proposed curve fitting method is demonstrated by compensating time shifts in ToF data of a coin due to the presence of tilt. The method is implemented for the correction of different amounts of tilt in the coin corresponding to angles 6.67°, 12.65° and 15.95°. It is observed that the present method can perform time offset correction in the time domain data of SAM with an accuracy of 45 arcsec. The experimental results confirm the effectiveness of the suggested tilt compensation technique in SAM, indicating its potential for future applications.

KEYWORDS
scanning acoustic microscopy, tilt correction, transducer, ultrasonic waves

1 | INTRODUCTION

Scanning acoustic microscopy (SAM) is a noninvasive and nondestructive imaging technology that has been used for surface and subsurface microscopic imaging of various objects, from industrial to biological specimens, for the last several decades.[1–5] SAM is a noninvasive and nondestructive technology widely used for surface and subsurface microscopic imaging of industrial objects and biological specimens. It is extensively used for microstructural characterisation, surface and subsurface mechanical properties characterisation of materials, structural health monitoring of composite structures, studies of phonon propagations, and detecting surface defects on polymer circuits.[6–13] At the same time, SAM also allows visualisation and determines the spatial distributional changes in

elasticity, density and viscosity of the sample.[14,15] Moreover, due to its ability to handle the intricate details of miniaturised assemblies such as chip-scale packages and 3D IC stacks, this tool has become increasingly vital in the industry.[16,17] In high-resolution SAM, ∼200 nm has been achieved by using a 4.4 GHz acoustic transducer.[18] SAM offers two significant advantages over other imaging modalities. First, it enables high-speed data acquisition in 2D maps, allowing for efficient imaging. Second, SAM allows for instantaneous scanning of industrial and biological samples without requiring staining or labelling, or extensive preparation, which is a major benefit. Another advantage of SAM, it has the ability to generate a 3D visualisation from a 2D scan of any kind of sample by incorporating ToF information. This is achieved by measuring the time delay of the reflected ultrasound waves, which provides depth/time information of the sample.

SAM operates in two different modes, pulse-echo mode and transmission mode, each of which generates acoustic signals collected at each point, and depth information is recorded in a 3D matrix format (spatial and temporal) using a raster/serpentine scanning motion of the transducer on the sample surface.[19,20] An ultrasonic image is formed by digitally compiling a series of A-scans obtained during lateral scanning of the sample. This is achieved by scanning the sample surface using a single/array acoustic lens and collecting three-dimensional data about the object's mechanical properties in the volume.

Acoustic microscopes produce two basic image formats, namely, B-scan and C-scan. Additionally, advanced data processing algorithms can generate enhanced images that belong to either of these two categories. C-scan images are generated by recording the amplitude and its corresponding time at a chosen depth range for each C-scan point. These images provide information about the sample's topography and material composition. However, to ensure the reliability of the conclusions drawn from C-scan images, one of the sample surfaces must be parallel to the transducer scanning plane to provide a suitable reference. Any deviation from this assumption can result in an incorrect conclusion about the sample, particularly in high-frequency acoustics imaging.

There are many commercially available SAM systems in the market, but they lack automatic inclination correction in their data processing software and hardware setup. Prakhar et al. proposed a tilt correction method that involves selecting three points on the same plane of the object, finding the angle of inclination, and correcting for artefacts caused by the inclination.[21] The correction of sample surface inclination is performed during the postprocessing phase of each A-scan in the time domain. However, this method has a limitation that it relies on prior knowledge of the sample's surface or shape and the exact position of the specimen's surface in space. Moreover, it also is necessary to select three possible points, which lie in the same plane, which is very difficult to choose in a nonuniform object. Rupitsch and Zager have employed an advanced SAM setup that allows investigating the specimens with curved surfaces or scanning planes that are not parallel to the holder, but authors did not claim any tilt correction in the acquired images.[22] Hillmann et al. have identified and corrected the tilt angle of the spherical sample by using a spatial dependence of the reflection coefficient for the sample.[23]

In recent decades, the fields of optical microscopy, image processing, and computer vision have dedicated themselves to rectifying aberrations and tilts.[24–29] Nevertheless, a significant gap remains in the lack of automated postprocessing tilt correction, applicable both commercially and in SAM images. This paper aims to bridge this void by presenting a transformative methodology to adjust sample inclination within SAM images. By using a new and creative method, this research aims to improve tilt correction. This could lead to exciting progress in the fields of microscopy and image processing.

2 | METHODOLOGY

2.1 | Background

The change in time of flight for each pulse or the increased attenuation in the medium is the primary cause of artefacts created by the inclination between the sample and the focal plane. A detailed explanation can be found in Ref. (21). Other elements, such as the transducer aperture and excitation pulse, impact the output image in addition to these critical variables. On the other hand, one can ignore secondary factors since the changes they cause are inextricably linked with the experimental design and cannot compensate for in data postprocessing.

The recorded 3D acoustic data are previewed using the maximum intensity projection by employing the volume viewer tool in MATLAB to visualise the tilt effectively. To achieve the proper perspective of the tilted coin, several sections and slices of the data are plotted first. In order to reduce the noise in the signal, the 3D data set is cropped around the maximum point of the mean data, resulting in a 3D cropped mean matrix, which is then applied to a proposed tilt removal algorithm. A flow chart shown in Figure 1 describes a complete workflow of the manuscript (Figure 2).

The initial step of the proposed tilt removal technique involves creating a binary mask. This mask is generated from the maximum valued array obtained in the *XZ* plane. Subsequently, the method works with individual filtered
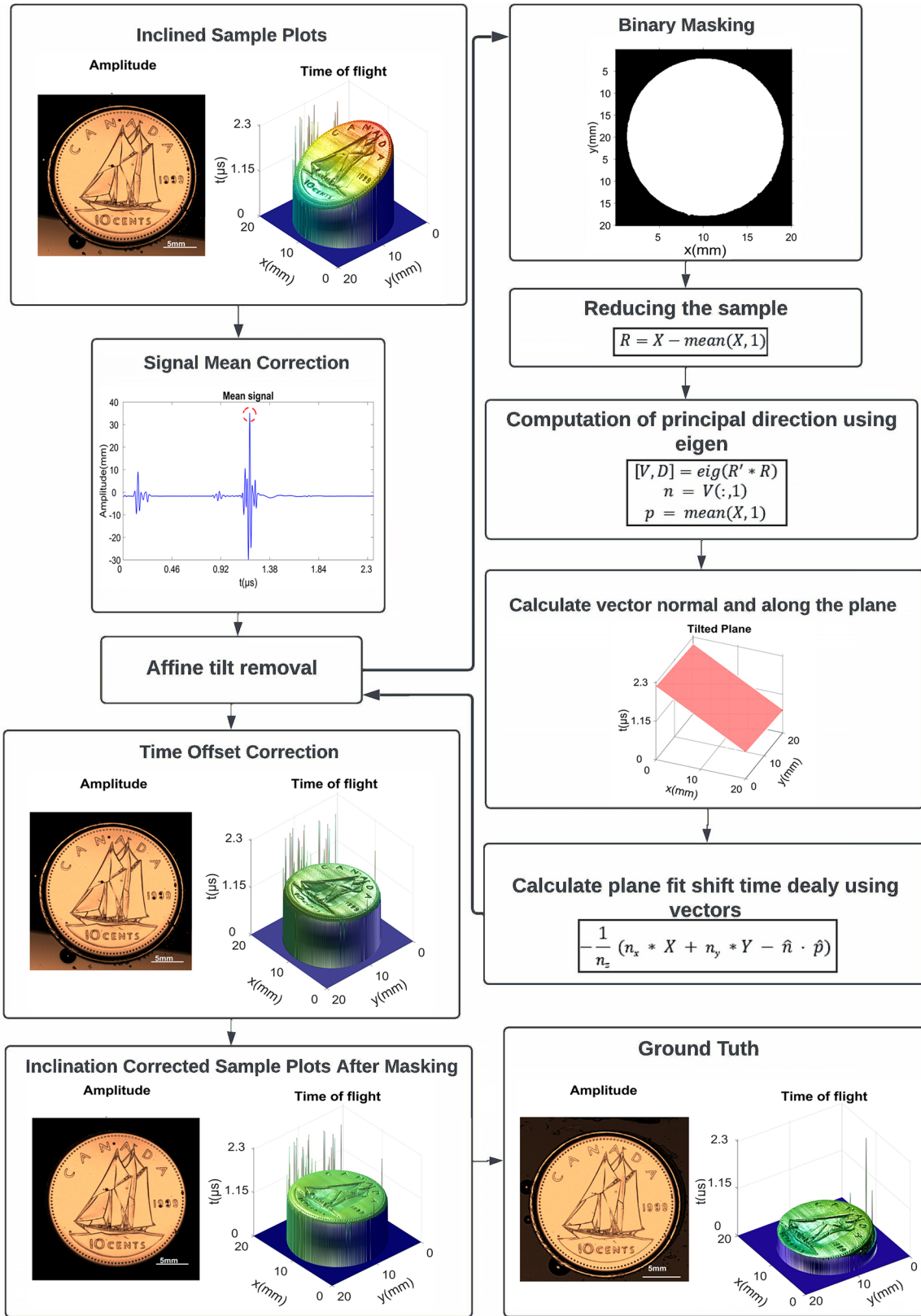
FIGURE 1 The depicted process flowchart succinctly summarises the sequential steps and methodology employed by the proposed algorithm for tilt correction. It offers a visual overview of how the algorithm progresses from input to output, highlighting the key stages involved in identifying and rectifying image inclination.
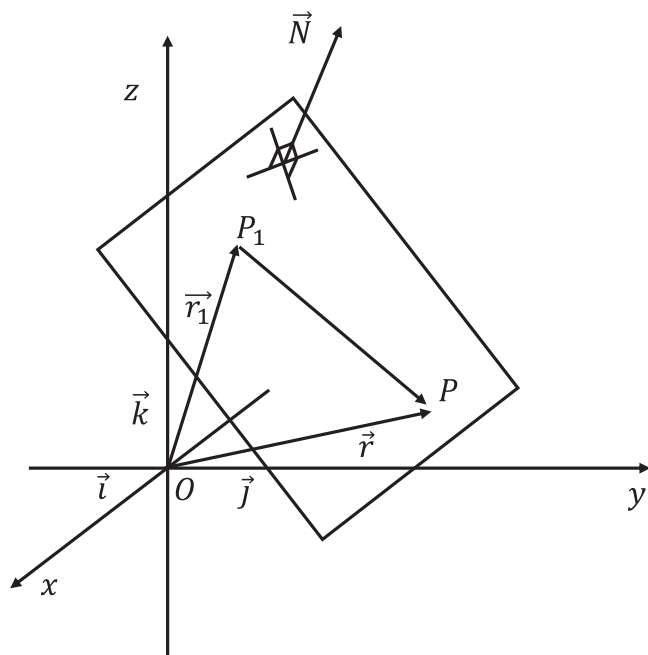
FIGURE 2 A graphical representation of a plane characterised by its normal vector, along with a marked point situated on the inclined plane. This visual depiction elucidates the interplay between the plane's orientation and the specific point's positioning, enhancing the conceptual understanding of their spatial relationship.

rows, columns and a matrix representing time shifts. For each of these, a transformation is performed, converting them into separate 3D arrays.

Following this transformation, the generated 3D data is subjected to a reduction process. This reduction is achieved by subtracting the transformed data from the mean data. This step is crucial for effectively removing the tilt component and achieving the desired correction in the dataset. The combination of these steps in sequence constitutes the core methodology employed to eliminate tilt artefacts from the data. The eigenvectors are then used to compute the plane's normal and points that belong to the plane. Then there is the time-delay matrix for the generation plane shift, which has points roughly in the $Z = X$ plane. This matrix is used to shift the time signals (z-axis) in the original data matrix by adding a particular time delay. Once again, the actual data matrix is passed through a mean correction to generate the final output data. The heatmap plot is computed utilising the maximum valued position array multiplied by the velocity of the ultrasonic beam employed and the time-of-flight matrix. The slope of the XZ tilted plane is used to compute the tilt angle. After generating the normal and in the plane, points using this proposed fitting plane are calculated and utilised. The delays are the differences in time between this intended plane and the reference plane. This eliminates inaccuracies in the phases

of the signals or their time of flight. To resolve the concerns raised above, a flowchart depicted in Figure 1 will be used.

2.2 | Sample data noise processing

When viewed as a whole, the bulk of the sample data contains a sizable degree of noise. To remove the noisy portion of the data, the mean value was used. This stage is undertaken to prepare the data for the process; data signals are produced, and the mean value is evaluated along the time scale. By visualising the mean of all the signals, the maximum amplitude of the mean is determined. We noticed that we had the least amount of noise in the data at the time. The signal was then cropped and reduced to a narrower range around the highest position value of the mean. The clipped signal is cleaner and more accessible to analyse than the original data stream.

2.3 | Proposed curve fitting

Acoustic microscope typically generates 3D data, where x and y dimensions represent the transducer scanning directions and z dimension represents the ToF information of the acoustic wave, also called A-scan at every x and y coordinates of the sample. ToF of the acoustic waves provides the information of height variation across the sample, which can be easily affected by either tilt in the sample or tilt in the scanning stage. The height measurement error introduced due to the tilt either in the sample or in the scanning stage need to be removed for faithful measurement. Proposed computational method which is a fully automatic and fast procedure to measure the unwanted tilt introduced in the 3D data of the sample and can be a useful tool for faithful height measurement of the sample. It requires some postprocessing steps for accurate estimation of the tilt in the 3D sample data.

The acoustic signal, that is, every A-scan has 1024 time points, which covers the span of ToF of the acoustic signal reflecting from the sample. Sometime, the entire ToF data has a time delay, which shifts some of the information of the sample to the opposite side of the time series data and introduces difficulty in the correct estimation of the tilt in the 3D recorded data. In order to avoid this, mean value of the ToF information corresponding to maximum amplitude of the acoustic signal across both x and y dimensions is measured and subtracted from every A-scan. The entire 3D data is then shifted to the middle of A-scan time points, that is, at 512 time point, along z dimension. Next, the amplitude image of the sample is generated by selecting the maximum amplitude values of every A-scan, which is further utilised to form the binary mask. The

binary mask is used to choose the ToF values corresponding to the maximum amplitude values of every A-scan within the domain of the sample. The regions falling outside the sample domain are not considered to estimate the tilt information in the 3D sample acoustic data.

The masked sample data and their coordinate values are rearranged along columns of a matrix 'P' of dimension $M \times 3$, where M is the number of data points within the masked region. First two columns of the matrix have X and Y coordinate values and the third column has corresponding maximum amplitude values of every A-scan. The column-wise mean (μ_{c_i}) values of the matrix are calculated and utilised to transform the matrix 'P' as follows:

$$R = \left[P_{c_i} - \mu_{c_i} \right], \tag{1}$$

where c_i represents ith column of matrix P.

The modified matrix 'R' is further utilised to compute the normal vector 'N' to the best fit plane and a point 'p' that belongs to the plane. We utilised MATLAB command 'eig' to compute a matrix 'V' whose columns are the right eigenvectors, a diagonal matrix 'D' of eigenvalues and the coordinates of the point 'p' which lie on the fitted plane. It can be written as follows:

$$[V, D, p] = eig\left(R' \times R\right). \tag{2}$$

The first column of the right eigenvector matrix 'V' represents the primary directions in the sample data points. Mathematically, it can be written as follows:

$$N = \left\langle V_{1,1}, V_{2,1}, V_{3,1} \right\rangle, \tag{3}$$

where $V_{1,1}$, $V_{2,1}$, $V_{3,1}$ are the unit vectors of a normal unit vector 'N' along x, y, z directions and can be represented by N_x, N_y and N_z (say).

The fitted plane is then represented by the following relation:

$$P_C = -\left[\frac{N_x}{N_z}X + \frac{N_y}{N_z}Y - \frac{N \cdot p}{N_z}\right]. \tag{4}$$

2.4 | Time offset correction

We correct the time shift present in the signals using the plane and the maximum index of the mean of the sample data along the time plane we discovered using the proposed fit in the time offset correction stage. We moved the data signals using that plane. In addition, we were eventually rectifying the phase of the data's time shift. The time shift is depicted in the diagram below.

$$P(i, j, t) = \text{circshift}\left(P(i, j, t), -\left(P_c(i, j) + \mu_{\text{max\_idx}}\right)\right). \tag{5}$$

By circular shifting or by doing the right rotation of the time signal using the plane coordinates and the maximum index of the mean of the sample data along the z-axis or the time plane, we can achieve the time correction for the given data.

In Figure 3a, the coin image plane appears to be tilted at an angle of approximately 12.65°. The vertical line in Figure 3a represents a reference point from which time shifts were measured. The points marked on Figure 3a plane indicate the positions where time shifts were selected for comparison between the images before (Figure 3b) and after (Figure 3c) the time-shift correction. The comparison between the two images (Figure 3b and c) reveals the improvement achieved by the correction.

The waves index fluctuates a lot as we travel down along the XY plane (i.e., first subplot shows at $X = 100$ pixels = 5 mm and $Y = 100$ pixels = 5 mm, similarly the last subplot shows at $X = 200$ pixels = 10 mm and $Y = 200$ pixels = 10 mm) before the time-shifting or correction of the time signal. The above procedure virtually corrects this, eventually rectifying the time shift.

2.5 | Simulation

To check the effectiveness of the proposed method for tilt removal, a systematic simulation study is performed and further compared with the manual tilt removal method.[21] A Gaussian structure on the plane of 200×200 pixels having intensity values with Gaussian noise of 10 units and a random seed of 200 is simulated. The simulated plane is then rotated by various angles of 2°, 5° and 10° as illustrated in Figure 4a–c. First, tilt error is compensated by employing manual tilt removal algorithm. For manual tilt removal method, three different x and y coordinates in a plane were randomly selected and corresponding coordinate values are given in $P1$ of Table 1. The coordinate values of three points on the simulated data were utilised for fitting the plane. The fitted plane is then subtracted from the simulated data for tilt error compensation as depicted in Figure 4d–f. In order to check the robustness of the manual tilt removal method, the above process is repeated for three different sets of x and y coordinates in a plane. In Table 1, the coordinates are denoted as $P1$, $P2$ and $P3$, with their respective values. The tilt compensated simulated data maps are illustrated in Figure 4g–l, respectively. Table 1 also provides the root mean square errors (RMSE) for $P1$, $P2$ and $P3$ at tilt angles of 2°, 5° and 10°, respectively. It can be seen that RMSE is found to be large and different for the chosen three different sets of x and y coordinates, suggesting inaccuracy in the tilt compensation. Next, tilted data sets corresponding to angles of 2°, 5° and 10° are compensated by employing a fully automated
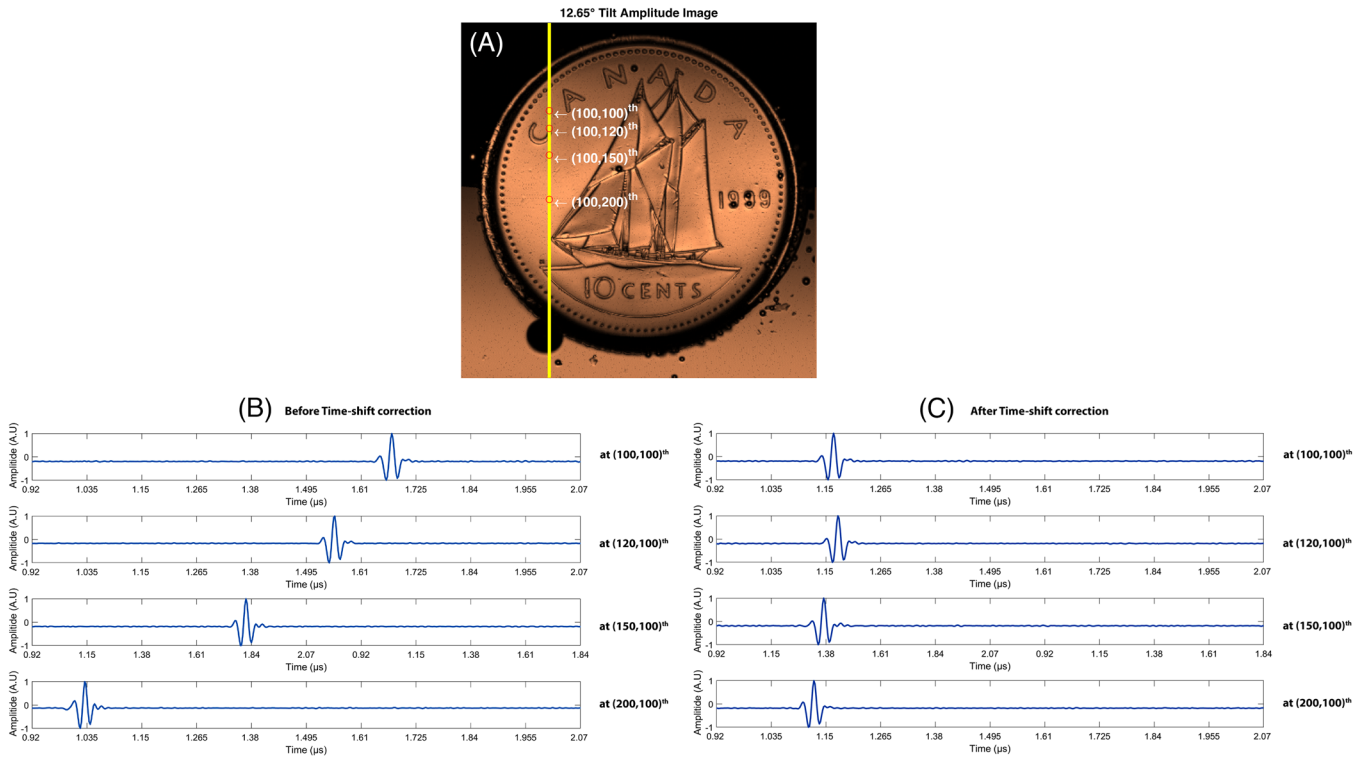
FIGURE 3   (a) A coin image plane that is tilted at an angle of 12.65°. The vertical line and the points in the figure indicate the positions where time shifts were selected for comparison between the images before and after the time-shift correction, as shown in (b) and (c), respectively.

TABLE 1   RMSE of the amount of tilt removed for both manual tilt removal method and proposed automated tilt methods were applied for 2°, 5° and 10°. Three different coordinates referencing to be *P1*, *P2* and *P3* were chosen to apply for the manual tilt removal method.

Theta		RMSE		
Method	**Coordinate sets**	**2°**	**5°**	**10°**
Manual	P1 [(64, 140), (149, 117), (62, 55)]	2.42	5.41	10.39
	P2 [(112, 177), (32, 49), (57, 4)]	2.46	5.47	10.46
	P3 [(24, 87), (34, 42), (150, 150)]	1.31	4.29	9.28
Proposed	Automated	1.16	1.12	1.02

proposed tilt compensation method. The corrected data maps are presented in Figure 4m–o. The RMSE associated with the proposed method remains consistently low and stable, in contrast to the manual tilt removal method, indicating that the proposed method is accurate and robust in mitigating tilt artefacts. The line profiles of the simulated tilted planes and corrected planes using both the manual and proposed method are illustrated in Figure 5a–l.

3 | EXPERIMENTAL SETUP

In Figure 6, a labelled image of SAM is presented. This imaging technique employs the reflection mode to capture images of the sample. Through this mode, SAM effectively unveils distinct characteristics of the sample's features. This manuscript strongly emphasises the use of the reflection mode for scanning samples. To achieve this, we use a curved sapphire lens rod. This lens rod acts as a pivotal component, serving to concentrate acoustic energy. This energy is then directed through a coupling medium, where water is employed in this specific case. This coordination of elements facilitates a meticulous concentration of acoustic energy, enabling the capture of images through the reflection mode in SAM. Ultrasonic signals are then produced by a signal generator and sent to the sample. Further details regarding the working principles of these modes can be found elsewhere.[30,31] After focusing the acoustic energy
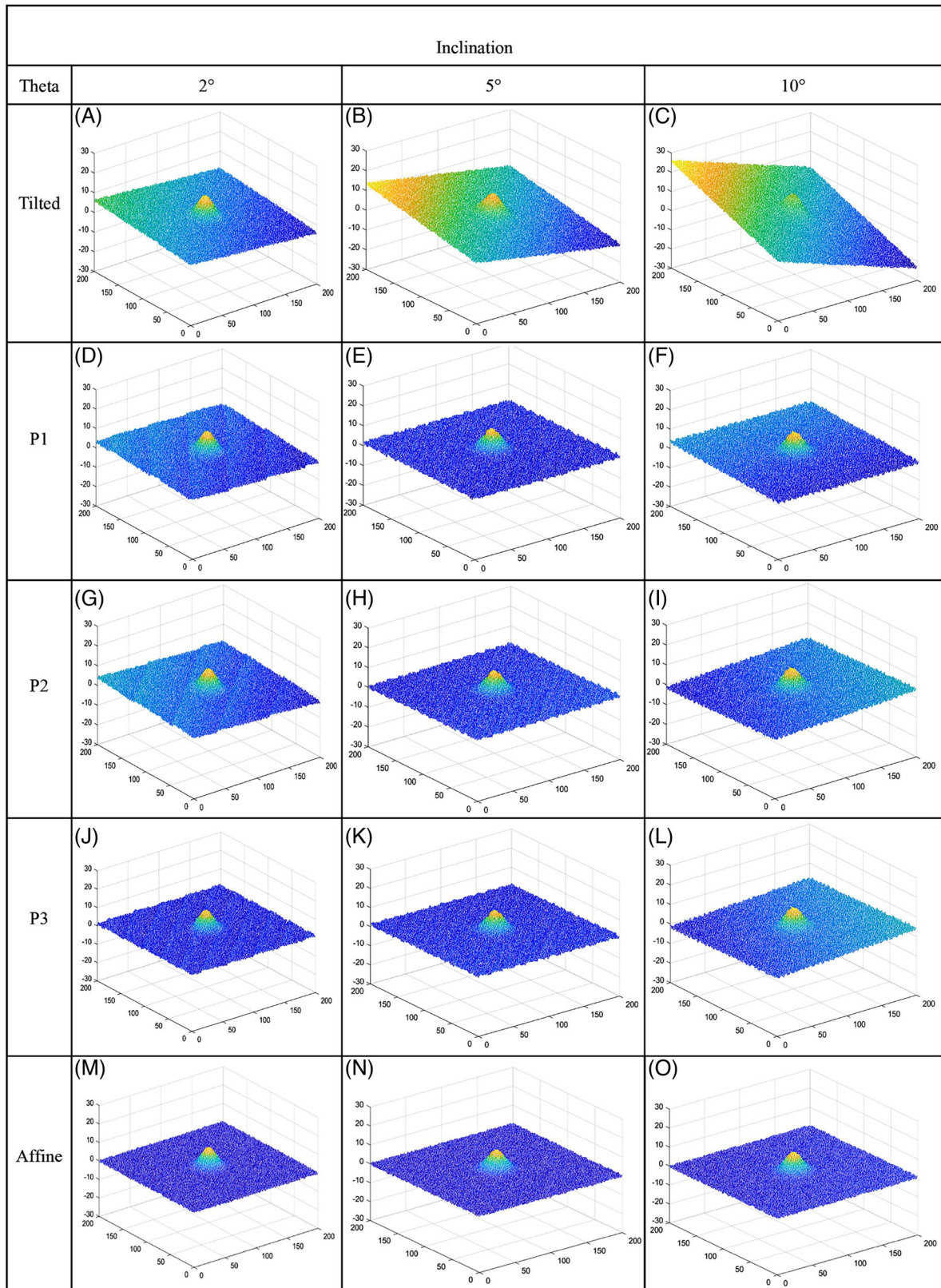
FIGURE 4 The diagram above shows the mesh of the simulation plane where both the manual tilt removal method and proposed automated tilt methods were applied for 2°, 5° and 10°. Three different coordinates referencing *P*1, *P*2 and *P*3 were chosen to apply for the manual tilt removal method.
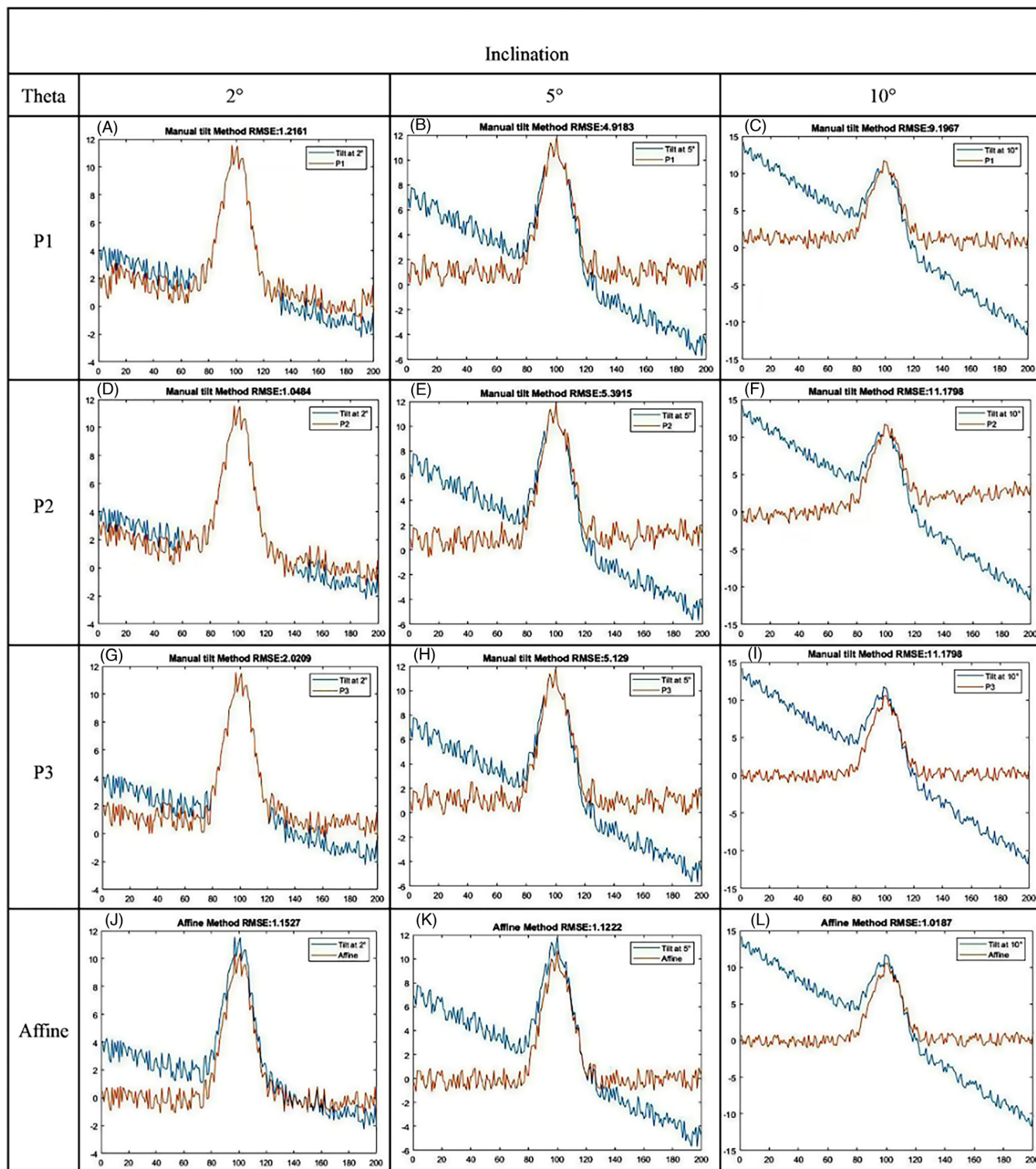
FIGURE 5 The diagram above shows the cross-section of the simulation plane where both the manual removal tilt method and proposed automated tilt methods were applied for 2°, 5° and 10°. Three different coordinates referencing *P*1, *P*2 and *P*3 were chosen to apply for the manual tilt removal method.

through a coupling medium, typically water, ultrasonic signals are generated towards the sample using a signal generator. These signals reflect back from the sample and are detected, resulting in an A-scan or amplitude scan.

To produce a C-scan image of the sample, this process is repeated at various positions in the *XY* plane. The C-scan can also be viewed as a two-dimensional composition of A-scans.
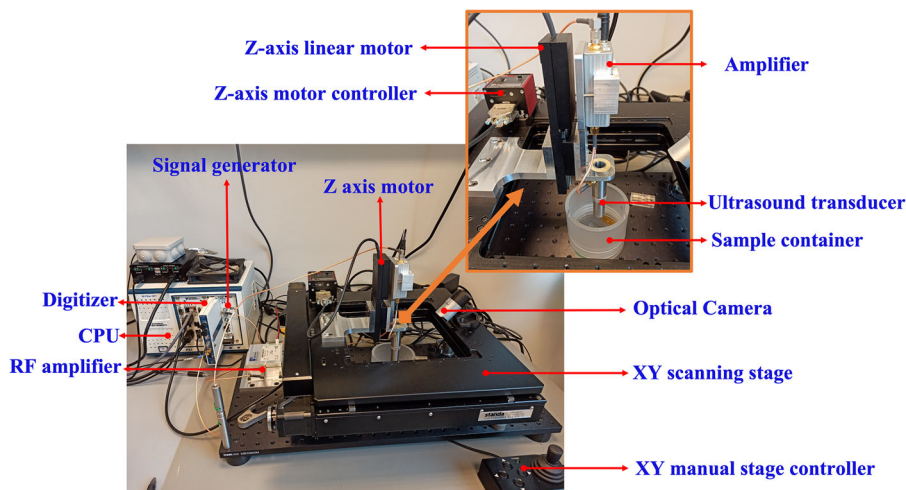
FIGURE 6 The depicted figure illustrates the labelled image of the SAM employed for image acquisition, as expounded in this paper. The experimental setup encompasses all the indispensable constituents that constitute a SAM system.
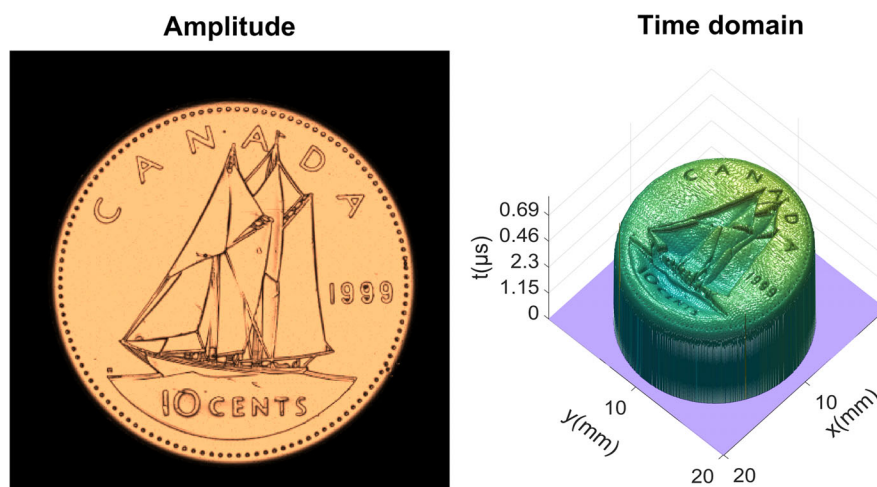

FIGURE 7 The graphic depicts sample data, 3D time signal mesh, a tilted plane, and two other planes on the top and bottom of the coin. This also shows how the k_{ij} matrix is evaluated. (The reader is directed to the online version of this article for interpretation of the colour references in this figure legend.)

The data acquisitions were conducted using a custom-built SAM that was integrated with a high-precision scanning stage (Standa 8MTF-200-Motorized XY Microscope Stage) and controlled by LabVIEW. Our group had previously utilised a similar SAM to identify and correct inclined samples, as reported in a previous study.[21] National Instruments' PXIe FPGA modules and FlexRIO hardware were utilised to implement the acoustic microscopic features. These were housed in a PXIe chassis (PXIe-1082), which included an arbitrary waveform generator (AT-1212).

To enhance the ultrasonic signals, the excited signals were directed towards an RF amplifier (AMP018032-T). For accurate reference measurements, an Olympus 50 MHz focused transducer, featuring a 6.35 mm aperture and a 12 mm focal length, was employed to perform scans across the samples. Following the reflection of ultrasonic waves

from the samples, the resultant signals underwent amplification using a purpose-built preamplifier. Subsequently, these signals were digitised through a high-speed 12-bit digitiser (NI-5772) with a sampling rate of 1.6 Gs/s. All experiments were conducted using distilled water, and the room temperature was maintained at a constant level. For ground truth and tilted imaging, the sample was mounted on a flat stage. The manual stage's position is controlled by a precision micrometre head that has a reading accuracy of 0.01 mm, with one division equivalent to a displacement of 20 arcsec.

4 | EXPERIMENTAL RESULTS

The experiments are conducted on Canada 10-cent coin using SAM depicted in Figure 6. The acoustic transducer
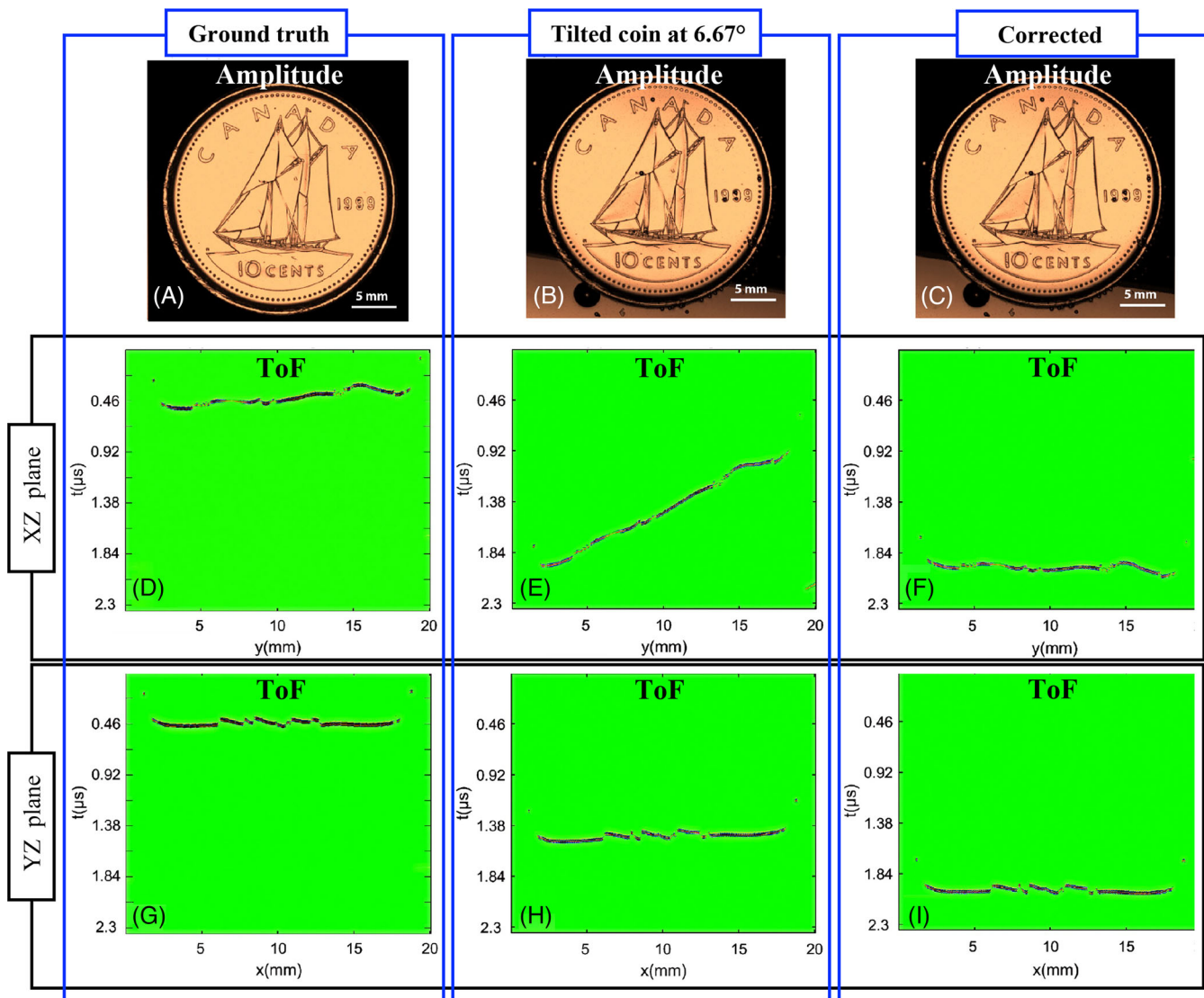
FIGURE 8 The figure depicts the before and after processing tilt correction of the coin using the proposed algorithm. (a) The first row shows the ground truth images of the coin from different planes with tilt (d) XZ plane, (g) YZ plane. The second row shows the tilted image (b) and its tilted planes (e) XZ plane, (h) YZ plane, respectively. (c) Tilt corrected images using the proposed algorithm and its corresponding corrected the planes (f) XZ plane and (i) YZ plane.

in the developed SAM is attached to a *XYZ* translation stage with travel ranges of 200 mm × 200 mm × 50 mm along *x*, *y* and *z* directions and the sample is kept stationary during the data acquisition. SAM instrument emits high-frequency ultrasound waves that are focused onto the sample. These waves penetrated into the sample and interacted with its internal structure. The transducer used for emitting and detecting ultrasound waves are positioned and aligned with the centre of the sample. The reflected ultrasound waves are then detected by the same transducer and converted into electrical signals. The detected signal contains depth information of the specimen, which is encoded in the time of flight of the ultrasound waves. To generates 3D data set of the coin, the sample is scanned along *X* and *Y* axis using the scanning stage as shown

in Figure 7. It is evident that the coin exhibits a discernible tilt, which could originate from either the tilt in the scanning stage or the sample platform.

Figure 8b and c illustrates the amplitude image of the coin before and after tilt compensation using the proposed method. The amplitude images are generated by projecting the maximum amplitude information of the coin, and as a result, the impact of the tilt cannot be discerned in the amplitude images. Whereas the effect of tilt can be easily observed in the time-of-flight XZ and YZ cross-sectional images of the coin. The time-of-flight cross-sectional images of the coin before and after tilt removal are illustrated in Figure 8e and f and h and i, respectively. It can be visualised that the proposed method of tilt compensation performed very well on the experimental data as well.
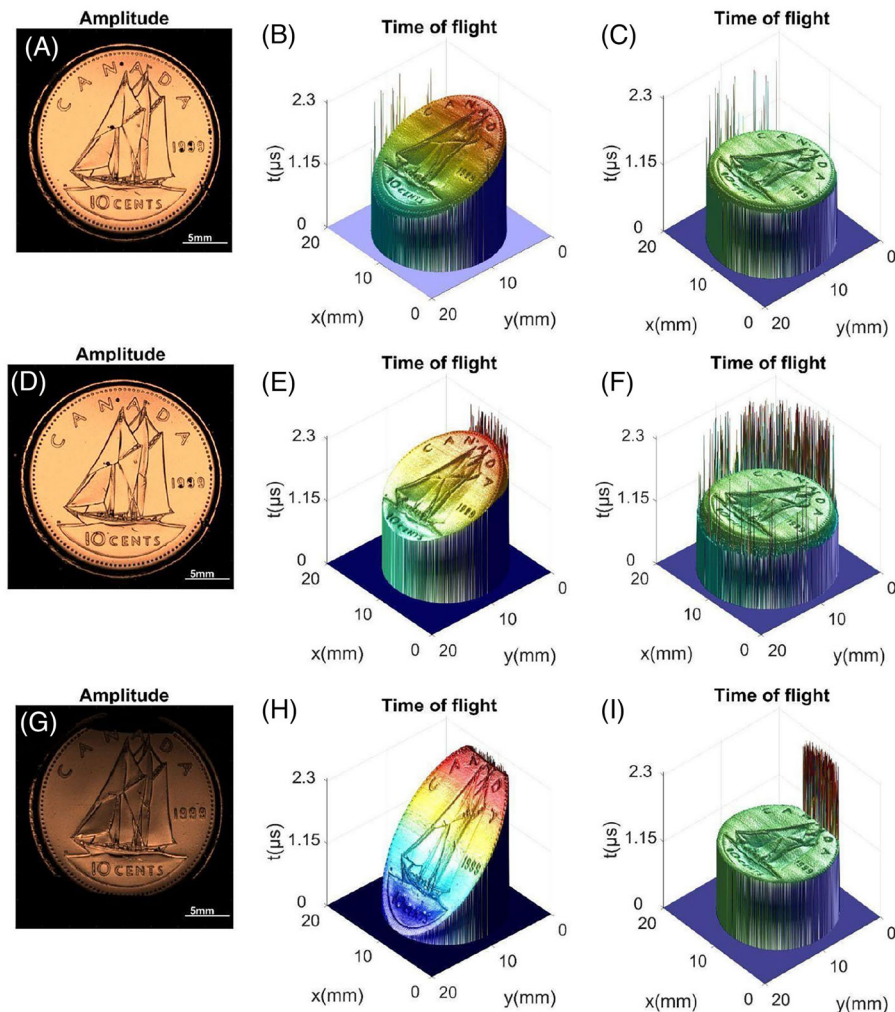
FIGURE 9 The figure depicts the before and after processing tilt correction of the coin using the proposed algorithm. The first subplot shows the sample data containing 1.5 mm tilt angle, the second subplot shows the sample data containing 4.5 mm tilt angle, and the last subplot denotes the sample data containing the 6 mm tilt angle.

Next, SAM experiments are conducted on the same coin, wherein different amounts of tilt are introduced in the sample platform to assess the efficacy of the proposed tilt compensation method. In order to introduce tilt in the sample, the coin is affixed to a mechanical platform that allows for precise control of tilt, with a minimum step size of 45 arcsec. The experimental data of the coin is then acquired corresponding to three different amount of tilt angles which corresponds to the vertical translation of 1.5, 4.5 and 6 mm in the sample platform. The reconstructed 3D time-of-flight data of the coin before and after tilt compensation corresponding to 1.5-, 4.5-, and 6-mm tilt angles are illustrated in Figure 9a–f, respectively. The proposed method for tilt compensation in the SAM data demonstrated effective results, indicating the potential of this approach. By introducing manual tilt in the sample platform during SAM experiments on the coin, the tilt error in the acquired data was successfully compensated.

This suggests that the proposed method has the capability to mitigate the impact of tilt, which can often introduce artefacts or inaccuracies in the SAM imaging process. Further analysis and validation of the results could potentially establish this approach as a reliable method for tilt compensation in SAM imaging of specimens with tilt-induced errors.

5 | CONCLUSION

The effectiveness of the proposed method in correcting tilt errors, whether caused by sample tilt or scanning stage tilt, has been demonstrated in comparison to the manual method. This means that even when the sample is inclined or tilted, the proposed method can accurately compensate for these errors, resulting in more accurate and reliable SAM images. This is particularly important when imaging

samples with complex or irregular geometries, where tilt-induced artefacts can significantly impact the quality and accuracy of the imaging results. The proposed method has been validated through both simulations and experiments, providing a comprehensive assessment of its effectiveness. Simulation studies allow for controlled testing of the method's performance, while experimental validation confirms its real-world applicability. The combination of simulation and experimental results adds robustness and reliability to the proposed method, strengthening its credibility for practical use in SAM imaging.

The proposed method is fully automated, which eliminates the need for manual intervention in the tilt compensation process. This not only saves time but also minimises the potential for human error. The method can be integrated into the SAM imaging process as a software-based solution, making it efficient and easy to implement in practical applications. The proposed method opens up possibilities for advanced SAM imaging applications in the future. For example, it could enable more precise and accurate imaging of complex samples with varying tilt angles, such as multilayered structures or samples with uneven surfaces. It could also facilitate the development of real-time or in situ SAM imaging techniques, where rapid and automated tilt compensation could enhance imaging performance. In addition, accurate tilt compensation can lead to improved data interpretation and analysis in SAM imaging. By eliminating or minimising tilt-induced artefacts, the proposed method can provide clearer and more reliable images, which can aid in better understanding and analysis of the internal structure of samples. This could have potential applications in various fields, including materials science, biology, electronics and more.

ACKNOWLEDGEMENTS

REFERENCES
1. Briggs, A., Briggs, G., & Kolosov, O. (2010). *Acoustic microscopy*. Oxford University Press.
2. Maev, R. G. (2013). *Advances in acoustic microscopy and high resolution imaging: From principles to applications – Advances in acoustic microscopy and high resolution imaging: From principles to applications*. Wiley.
3. Mohamed, E. T. A., & Declercq, N. F. (2020). Giga-Hertz ultrasonic microscopy: Getting over the obscurity – A short review on the biomedical applications. *Physics in Medicine*, *9*, 100025.
4. Hartfield, C. D., Moore, T. M., & Brand, S. (2019). Acoustic microscopy of semiconductor packages. In T. Gandhi (Ed.), *Microelectronics failure analysis desk reference* (p. 67). ASM International.
5. Habib, A., Vierinen, J., Islam, A., Martinez, I. Z., & MelandsØ, F. (2018). In vitro volume imaging of articular cartilage using chirp-coded high frequency ultrasound. In *2018 IEEE International Ultrasonics Symposium (IUS)* (pp. 1–4). IEEE.
6. Brand, S., Raum, K., & Czurratis, P. (2008). Scanning acoustic microscopy an application for evaulating varnish layer conditions non-destructively. In *2008 IEEE Ultrasonics Symposium* (pp. 615–618). IEEE.
7. Weglein, R. D., & Wilson, R. G. (1978). Characteristic material signatures by acoustic microscopy. *Electronics Letters*, *14*(12), 352–354. https://doi.org/10.1049/el:19780238
8. Kundu, T., Bereiter-Hahn, J., & Hillmann, K. (1991). Measuring elastic properties of cells by evaluation of scanning acoustic microscopy V (Z) values using simplex algorithm. *Biophysical Journal*, *59*(6), 1194–1207.
9. Habib, A., Shelke, A., Vogel, M., Pietsch, U., Jiang, X., & Kundu, T. (2012). Mechanical characterization of sintered piezo-electric ceramic material using scanning acoustic microscope. *Ultrasonics*, *52*(8), 989–995. https://doi.org/10.1016/j.ultras.2012.07.011
10. Habib, A., Shelke, A., Vogel, M., Brand, S., Jiang, X., Pietsch, U., Banerjee, S., & Kundu, T. (2015). Quantitative ultrasonic characterization of c-axis oriented polycrystalline AlN thin film for smart device application. *Acta Acustica United with Acustica*, *101*(4), 675–683. https://doi.org/10.3813/aaa.918863
11. Hofmann, M., Pflanzer, R., Habib, A., Shelke, A., Bereiter-Hahn, J., Bernd, A., Kaufmann, R., Sader, R., & Kippenberger, S. (2016). Scanning acoustic microscopy – A novel noninvasive method to determine tumor interstitial fluid pressure in a xenograft tumor model. *Translational Oncology*, *9*(3), 179–183. https://doi.org/10.1016/j.tranon.2016.03.009
12. Wagle, S., Habib, A., & Melandsø, F. (2017). Ultrasonic measurements of surface defects on flexible circuits using high-frequency focused polymer transducers. *Japanese Journal of Applied Physics*, *56*(7S1), 7JC05–NA. https://doi.org/10.7567/jjap.56.07jc05
13. Morokov, E., Levin, V., Chernov, A., & Shanygin, A. (2021). High resolution ply-by-ply ultrasound imaging of impact damage in thick CFRP laminates by high-frequency acoustic microscopy. *Composite Structures*, *256*, 113102.
14. Dahmani, H., Zaaroura, I., Salhab, A., Campistron, P., Carlier, J., Toubal, M., Harmand, S., Thomy, V., Neyens, M., & Nongaillard, B. (2020). Fabrication and optimization of high frequency ZnO transducers for both longitudinal and shear emission: Application of viscosity measurement using ultrasound. *Advances in Science, Technology and Engineering Systems Journal*, *5*(6), 1428–1435.
15. Morokov, E. S., Demina, V. A., Sedush, N. G., Kalinin, K. T., Khramtsova, E. A., Dmitryakov, P. V., Bakirov, A. V., Grigoriev, T. E., Levin, V. M., & Chvalun, S. N. (2020). Noninvasive high-frequency acoustic microscopy for 3D visualization of microstructure and estimation of elastic properties during hydrolytic degradation of lactide and ε-caprolactone polymers. *Acta Biomaterialia*, *109*, 61–72.
16. Abadie, K., Montméat, P., Enot, T., Fournel, F., & Wimplinger, M. (2019). Application of temporary adherence to improve the

manufacturing of 3D thin silicon wafers. *International Journal of Adhesion and Adhesives*, *91*, 123–130.

17. Yazdan Mehr, M., Bahrami, A., Fischer, H., Gielen, S., Corbeij, R., van Driel, W. D., & Zhang, G. Q. (2015). An overview of scanning acoustic microscope, a reliable method for non-destructive failure analysis of microelectronic components. In *16th International Conference on Thermal, Mechanical and Multi-Physics Simulation and Experiments in Microelectronics and Microsystems* (pp. 1–4). IEEE.

18. Hadimioglu, B., & Quate, C. F. (1983). Water acoustic microscopy at suboptical wavelengths. *Applied Physics Letters*, *43*(11), 1006–1007. https://doi.org/10.1063/1.94223

19. Maev, R. G. (2008). *Acoustic microscopy: Fundamentals and applications*. John Wiley & Sons.

20. Briggs, A., & Kolosov, O. (2010). *Acoustic microscopy*. Oxford University Press.

21. Kumar, P., Yadav, N., Shamsuzzaman, M., Agarwal, K., Melandsø, F., & Habib, A. (2022). Numerical method for tilt compensation in scanning acoustic microscopy. *Measurement*, *187*, 110306.

22. Rupitsch, S. J., & Zagar, B. G. (2007). Acoustic microscopy technique to precisely locate layer delamination. *IEEE Transactions on Instrumentation and Measurement*, *56*(4), 1429–1434. https://doi.org/10.1109/tim.2007.899866

23. Hillmann, K., Grill, W., & Bereiter-Hahn, J. (1994). Determination of ultrasonic attenuation in small samples of solid material by scanning acoustic microscopy with phase contrast. *Journal of Alloys and Compounds*, *211–212*, 625–627. https://doi.org/10.1016/0925-8388(94)90582-7

24. Rodríguez, M., Delon, J., & Morel, J.-M. (2018). Covering the space of tilts. Application to affine invariant image comparison. *SIAM Journal on Imaging Sciences*, *11*(2), 1230–1267.

25. Copeland, C. R., McGray, C. D., Ilic, B. R., Geist, J., & Stavis, S. M. (2021). Accurate localization microscopy by intrinsic aberration calibration. *Nature Communications*, *12*(1), 3925.

26. Kumar, M., & Kozorovitskiy, Y. (2019). Tilt-invariant scanned oblique plane illumination microscopy for large-scale volumetric imaging. *Optics Letters*, *44*(7), 1706–1709.

27. Lee, J. H., Park, J. H., Jeong, D., Shin, E. J., & Park, C. (2016). Tip/tilt-compensated through-focus scanning optical microscopy. In *Optical metrology and inspection for industrial applications IV* (vol. 10023, pp. 118–123). SPIE.

28. Hawkes, P. (2009). Aberration correction past and present. *Philosophical Transactions of the Royal Society A: Mathematical, Physical and Engineering Sciences*, *367*(1903), 3637–3664.

29. Jones, L., Yang, H., Pennycook, T. J., Marshall, M. S. J., Van Aert, S., Browning, N. D., Castell, M. R., & Nellist, P. D. (2015). Smart Align – A new tool for robust non-rigid registration of scanning microscope data. *Advanced Structural and Chemical Imaging*, *1*(1), 1–16.

30. Maev, R. G. (2013). *Advances in acoustic microscopy and high resolution imaging: From principles to applications*. John Wiley & Sons.

31. Gupta, S. K., Pal, R., Ahmad, A., Melandsø, F., & Habib, A. (2023). Image denoising in acoustic microscopy using block-matching and 4D filter. *Scientific Reports*, *13*(1), 13212.